

Open camera or QR reader and  
scan code to access this article  
and other resources online.



# Lightweight Pneumatically Elastic Backbone Structure with Modular Construction and Nonlinear Interaction for Soft Actuators

Yang Yang,<sup>1-3</sup> Jiewen Lai,<sup>1</sup> Chaochao Xu,<sup>2,4</sup> Zhiguo He,<sup>3</sup> Pengcheng Jiao,<sup>3</sup> and Hongliang Ren<sup>1,2,4,5</sup>

## Abstract

There has been a growing need for soft robots operating various force-sensitive tasks due to their environmental adaptability, satisfactory controllability, and nonlinear mobility unique from rigid robots. It is of desire to further study *the system instability* and *strongly nonlinear interaction phenomenon* that are the main influence factors to the actuations of lightweight soft actuators. In this study, we present a design principle on lightweight pneumatically elastic backbone structure (PEBS) with the modular construction for soft actuators, which contains a backbone printed as one piece and a common strip balloon. We build a prototype of a lightweight (<80 g) soft actuator, which can perform bending motions with satisfactory output forces ( $\sim 20$  times self-weight). Experiments are conducted on the bending effects generated by interactions between the hyperelastic inner balloon and the elastic backbone. We investigated the nonlinear interaction and system instability experimentally, numerically, and parametrically. To overcome them, we further derived a theoretical nonlinear model and a numerical model. Satisfactory agreements are obtained between the numerical, theoretical, and experimental results. The accuracy of the numerical model is fully validated. Parametric studies are conducted on the backbone geometry and stiffness, balloon stiffness, thickness, and diameter. The accurate controllability, operation safety, modularization ability, and collaborative ability of the PEBS are validated by designing PEBS into a soft laryngoscope, a modularized PEBS library for a robotic arm, and a PEBS system that can operate remote surgery. The reported work provides a further applicability potential of soft robotics studies.

**Keywords:** soft robots, biomedical engineering, nonlinear interactions, numerical simulation, pneumatic actuation

<sup>1</sup>Department of Electronic Engineering, The Chinese University of Hong Kong, Hong Kong, China.

<sup>2</sup>Department of Biomedical Engineering (BME), National University of Singapore, Singapore, Singapore.

<sup>3</sup>Institute of Port, Coastal and Offshore Engineering, Ocean College, Zhejiang University, Zhoushan, Zhejiang, China.

<sup>4</sup>Research Institute, National University of Singapore (Suzhou), Suzhou, Jiangsu, China.

<sup>5</sup>Shun Hing Institute of Advanced Engineering, The Chinese University of Hong Kong (CUHK), Hong Kong, Hong Kong, China.

## Introduction

**S**OFT ROBOTS, WHICH are expected to address the challenges of traditional rigid robots on inflexible motions, have been reported with environmental adaptability and satisfactory human–robot interaction capability due to the nonlinear actuation mechanism.<sup>1,2</sup> Various soft robots are invented to meet requirements in different scenarios, such as soft grippers for gently grasping objects with irregular shapes,<sup>3–9</sup> soft jumpers for rapidly leaping over rough terrains,<sup>10–12</sup> and biomimetic soft robots for performing more environmentally adaptable motions.<sup>13–17</sup>

As one of the typical designs, soft actuators have been widely studied as the continuum structures generate impressive flexible motions. From the biomedical engineering perspective, the soft continuum actuator can be used for shape sensing in minimally invasive surgeries, making challenging clinical procedures possible with miniaturized instrumentation and high curvilinear access capabilities.<sup>18,19</sup> From the field exploration perspective, a three-degree-of-freedom (DOF) soft actuator grasped in shallow water and collected seafood animals at the bottom of the natural oceanic environments.<sup>20</sup> Moreover, from the automation engineering perspective, the soft harvesting robot can pick crops by adapting vine shapes automatically.<sup>21</sup>

Functional driving methods and smart structure designs are two main factors that constitute the actuation principles of these soft actuators. Driving methods in the form of power sources for the actuation processes include the fluidic actuation,<sup>7,22–24</sup> the cable actuation,<sup>8,25–28</sup> and the shape memory actuation.<sup>9,29,30</sup> Regarding smart structure designs, soft actuators can perform predefined deformations (e.g., bending) by utilizing the functional driving method providing powers that act on the designed structures and further generate anisotropic mechanical responses (e.g., backbone structures,<sup>31–33</sup> tentacles structures,<sup>34,35</sup> and fiber-reinforced structures<sup>36–38</sup>).

Benefiting from low-density soft materials, soft actuators are endowed with lightweights to perform gentler and more environmentally adaptable motions than rigid actuators. Masses of existing lightweight soft actuators range from ~10 g to 1 kg, which depends on structure designs and material selections. For example, fiber-reinforced soft actuators output forces more than 10 N by several hundred kilopascals of air-pressure inputs,<sup>36–38</sup> while their coil and molding fabrications are complex and tricky to be repaired after damage. Dielectric Elastomer actuated lightweight soft actuator (~18 g) can flexibly lift a ping-pong ball (~2.7 g),<sup>39</sup> while the payload could be further improved to realize practical applications. The pneumatic continuum soft arm (~1.12 kg) can output payloads of 4.6–6.7 times body-weight,<sup>40</sup> while the system mass is desired to be reduced to perform environmental adaptive tasks.

These cases reveal the fact that, to meet the output forces requirements, structure designs are usually at the expense of increasing system masses, limiting the applicability and mobility of the soft actuators in application scenarios of confined spaces. Soft actuators' applications propose requirements, such as light body weight, satisfactory payloads, and easy fabrication methods for assembly and modularization. Namely, to meet these requirements, the system instability and the strongly nonlinear interaction phenomenon during the actuation of lightweight actuators should be further studied.<sup>41</sup>

The system instability, which indicates a different implication from other research areas, is defined as undesirable performances (e.g., bulking fail of film actuators,<sup>39</sup> rupture fail of channel actuators,<sup>7,22–24</sup> fracture of fiber-reinforced actuators,<sup>36–38</sup> and so on) occurred due to the under improving load capability of lightweight soft actuators. In this study, we present a pneumatically elastic backbone structured (PEBS) soft actuator with modular construction whose system instability is investigated and overcome.

From the soft robotics perspective, this work provides a series of soft actuator designs with lightweight (8–80 g) and satisfactory payloads (~20 times self-weight), which play a role that remains the lightweight and high payloads, simultaneously. From the mechanical science perspective, this work investigates the mechanism of the strongly nonlinear interaction phenomenon between the classic elastomer and hyperelastomer. Derivations of the instability are investigated by mechanically analyzing the actuation process. Methods to overcome the instability are parametrically studied by considering the backbone geometry and stiffness, balloon stiffness, thickness, and diameter. From the engineering application perspective, this work is demonstrated with satisfactory modularization and applicability.

Due to the simple structure and the available components (commercial strip balloons and thermoplastic polyurethane [TPU] printing materials), PEBS can be easily fabricated, modularized, and assembled, compared with fiber-reinforced actuators, etc. At the same time, PEBS can output satisfactory payloads and gentle motions that are significantly required by biomedical engineering. We successfully modularized PEBS onto a robot arm and built a PEBS library. Furthermore, we applied the modularized PEBS to operate flexible laryngoscopy, gentle grasping/twisting, and remote operation.

This article is organized as follows: Design and Experiments section presents the design principle, the experimental test, and the output force evaluation of the soft actuator to address how the PEBS is actuated. Numerical Simulations section develops numerical simulations to investigate the nonlinear actuation mechanism of the soft actuators to address how the backbone and inner balloon nonlinearly interact with each other. Parametric Study section conducts the parametric study to geometrically address how the system instability is derived and to be overcome. Applications section demonstrates applications of PEBS to validate their applicability. Finally, Conclusions section concludes this work.

## Design and Experiments

### Design principle

Figure 1a illustrates the dimensions and detailed structures of the actuators. The actuators are endowed with lightweights (up to 80 g, including an inner balloon, a backbone structure, and a base) from a simple structure design, including a backbone, an inner balloon, and a tube. The backbone consists of a head that prevents axial expansions of the inner balloon, 20 semiring-shaped ribs that prevent radial expansions of the balloon, a base that provides a fixed constrain to the actuator, and a back wall connecting the above-mentioned parts while forming an asymmetric structure that transforms the balloon's isotropic expansions into actuator's anisotropic deformations (bending motions). The inlet side of the balloon is fixed and concentrically set inside the backbone. The tube

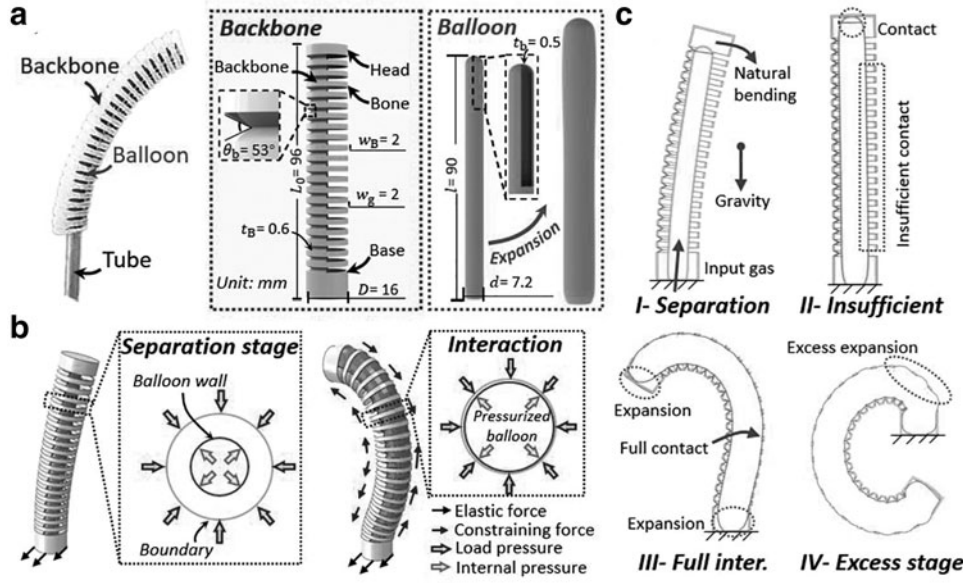


**FIG. 1.** Illustrative demonstration of the PEBS: (a) the detailed structure and dimensions of the PEBS, (b) the design principle that can be divided into the separation stage and the interaction stage, and (c) the design principle that can be specifically divided into the separation stage, the insufficient interaction stage, the full interaction stage, and the excessive interaction stage, based on the interaction conditions. PEBS, pneumatically elastic backbone structure.

is used for inputting air to expand the balloon. Note that the tube and the inlet side of the balloon are connected and well-sealed. The curved corrugations (see the corrugations in Fig. 1a) are designed to improve bending performance instead of using simpler and narrower flat strips to connect the ribs (rings).

The overall bending results from an accumulation of bendings between individual rib (ring) units. The curved corrugations transform bendings (flat strips perform) into foldings, thus amplifying the bending between individual rib (ring) units and further enhancing the overall bending performance. Moreover, the number of ribs is 20, which is determined by the dimensions of corrugations and the backbone structure (see dimensions in Fig. 1a).

Figure 1b illustrates the mechanical principle of the PEBS' actuation. The actuation process can be regarded as two main stages: separation and interaction. Regarding the separation stage, due to a 6 mm height and an 8.8 mm diameter difference, deformations of the backbone and balloon only develop with gravity. Affected by structural asymmetry, the backbone bends to the opposite side of the back wall. Furthermore, the bent backbone forces the balloon, which should be in an ideal upright state, to bend in the same direction. As the pressure inside the balloon increases, the balloon simultaneously expands radially and axially, and the separation stage ends when the balloon and backbone contact each other at the inner surface of the backbone's head.

Based on the contact conditions, the interaction stage can be divided into three substages: the insufficient interaction stage, the sufficient interaction stage, and the excessive interaction stage (Fig. 1c). During the insufficient interaction stage, the balloon performs a radial-direction-dominated expansion to contact the inner surfaces of the ribs (a space filling-up process) while deforming the backbone against natural bending. The sufficient interaction stage starts when the balloon fully touches the inner surfaces of the ribs. Due to the uneven distributions of bending stresses on both the rib and back wall sides, actuators perform obvious bending motions. However, as excess gas is input, the balloon surface will be expanded out of the backbone structure through gaps

between ribs leading to failures, which is the excess interaction stage.

Note that, in this work, we proposed a more generalized case with engineering error tolerances, instead of making the balloon fit the size of the backbone. The difference between the proposed generalized case and the fit-size case only considers the separation stage. The separation stage explains what will happen when a commercially obtained balloon is narrower than a backbone structure whose size is fixed for certain reasons (e.g., application requirements and so on).

### Experimental setup

Figure 2a shows the experimental setup containing a PEBS soft actuator, a base, a gas path system, and a differential pressure gauge. The gas path system contains three tubes connected by a tee connector that isobarically distributes the input gas into the actuator and the pressure gauge. The actuator and tube are, respectively, mounted on the top and bottom of the base. It should be noted that instead of fully printing the entire actuator, this modular construction design can reduce the bodyweight of the soft robot, and reduce the cost of failures (i.e., replace the inner balloon and backbone after ruptures and rib breakages, respectively), and simplify the assembly process. The input pressure varies from 0 to 80 kPa (operational limit in this work), and the corresponding bending motions of the actuator are recorded by an optical capture system.

To provide a generalized case, we selected the commercially obtained latex strip balloons (260Q; The Very Best Balloons, Qualatex, Canada) with a diameter-length-thickness of 7.2–90–0.5 mm. The backbone structure is printed as one piece by a Fused Deposition Manufacturing printer (Raise 3D Technologies, Inc., Irvine, CA, USA). During the printing, necessary printing supports are applied to the gaps between ribs.<sup>41–43</sup>

We considered two types of printing materials: thermoplastic elastomer (TPE) and TPU. TPE is a type of plastic material with hyperelastic characteristics and can stretch up

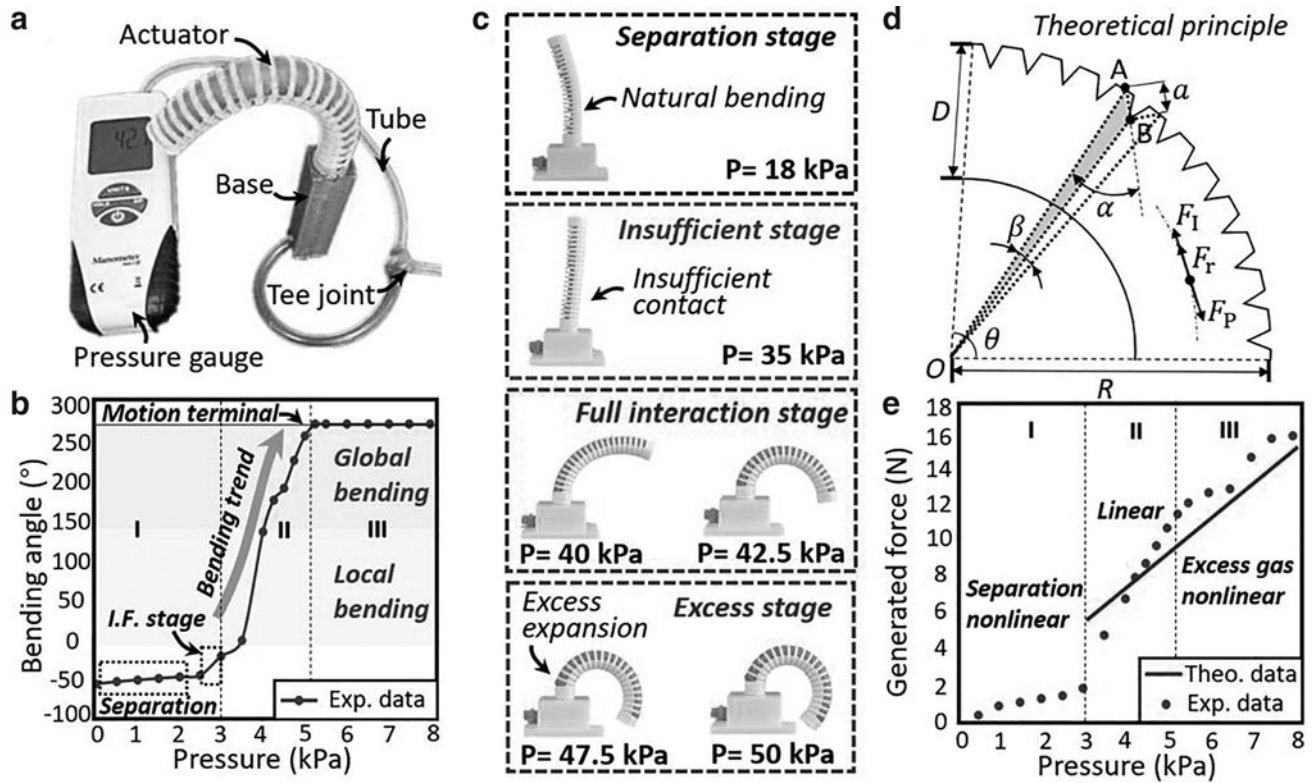


**FIG. 2.** Experimental setup and results: (a) the experimental setup of the bending tests, (b) results of the bending tests which show the bending motions the actuators perform start from  $\sim -50^\circ$  and end at  $270^\circ$ , (c) captured photographs showing performances of the actuators in different interaction stages, (d) the theoretical principle for external loads illustrating the finite unitization method and detailed geometric parameters, where the bellows represent the corrugation structure, and (e) comparisons between the theoretical and experimental results of the external loads, which show acceptable agreements and can be divided into the nonlinear separation state, the linear state, and the excessive gas nonlinear state, based on the characteristics of pressure-external load relationships.

to twice its original length while maintaining the ability to revert to its original form without plastic deformation.<sup>44,45</sup> However, it has a shore hardness of only 85 A, making it too soft to work with. In comparison, TPU is a higher durometer elastomer that can be regarded as the transition between rubbery thermoplastics and rigid plastics, making TPU a great replacement for hard rubber.<sup>46,47</sup> According to the reported mechanical principles, to simultaneously take the flexibility and stretch resistance of the backbone structure into account, TPU (eSUN 1.75 mm TPU, Shenzhen, China) is selected with a shore hardness of 94 A.

Note that Young's modulus is also a parameter that influences the bending performances of the PEBS. In this study, Young's modulus of the TPU material we used is 180 MPa (see more material information in Table 1). The applicable range of Young's modulus and its influence on bending performances are provided and discussed in Parametric Study section.

#### Experimental results

Figure 2b and c presents the actuation process obtained from the bending experiment, consistent with the reported design principle. Note that, we evaluated the bending performances of the actuators by measuring bending angles, which are angles between the vertical outward direction of the head and the plumb line. To measure output forces, a force gauge meter was applied in conjunction with the above-mentioned experimental system.

In the separation stage, bending angles were kept in the negative bending condition due to the responses of the backbone structure to gravity. It should be noted that a slight resilience tendency was observed during this stage. It reveals that, as the pressure increased, the balloon gradually lost contact with the ribs due to the expansion, and the backbone structure, therefore, returned to its original shape because it no longer bore the balloon's weight.

TABLE 1. DETAIL SETUPS OF NUMERICAL MODEL

Objects	Setup items	Values
Backbone	Density ( $\text{kg/m}^3$ )	$1.4 \times 10^3$
	Young's modulus (Pa)	$1.8 \times 10^8$
	Poisson's ratio	0.45
	Mesh size (m)	$8.9 \times 10^{-4}$
	Mesh method	Struct.
	Number of elements	7998
Channel	Density ( $\text{kg/m}^3$ )	$1.08 \times 10^3$
	Material para. C10 (Pa)	$1.6 \times 10^5$
	Incomp. para. D1 ( $\text{Pa}^{-1}$ )	$5.2 \times 10^{-4}$
	Mesh size (m)	$1 \times 10^{-3}$
	Mesh type	Struct. + Tet
	Number of elements	2087
Assembly	Interaction type	Full contact
	Step time (s)	1

In the insufficient stage, the balloon's expansion only acted on the inner surface of the head and provided the backbone structure with a thrust perpendicular to the surface. This effect resisted the gravity response of the backbone structure to return to its vertical state. During this period, the balloon kept expanding radially and finally touched the inner surfaces of the ribs.

In the sufficient interaction stage, the actuator performed satisfactory bending motions. Bending angles during this stage reached 0–180° showing satisfactory flexibilities of the PEBS. Excessive balloon expansions can be observed (see green-framed content in Fig. 2c). The head finally touched the side boundary of the wall, representing the end of the whole actuation process. Furthermore, continuing to pressurize the balloon led to failures, such as ribs breakages or balloon ruptures.

According to the pressure-angle relation, the whole actuation process can also be divided into three states (Fig. 2b). In state-I, a strongly nonlinear relation showed an irregularity of the balloon-backbone interaction phenomenon. In state-II, as observed, it showed an approximately linear relation. Furthermore, in state-III, the actuators stopped bending due to the limitation of the base. In general, it simultaneously reveals PEBS' advantages in satisfactory controllability (state-II) and disadvantages in system instability (state-I and

state-III), respectively. Furthermore, we explained the derivation of the system instability and investigated methods to overcome it in Numerical Simulations and Parametric Study sections.

A simplified theoretical model was established to estimate generated forces, which is validated by conducting a series of loading tests (see results in Fig. 2d, e and see detailed analysis in Supplementary Data).

## Numerical Simulations

### Numerical setup

To further understand how the backbone structure and the inner balloon nonlinearly interact with each other, the actuation process of the PEBS actuator is simulated in ABAQUS.<sup>48</sup> The phenomenon can be numerically described as: an elastomer (i.e., the backbone structure) is interacted with and deformed by expansions of a hyperelastomer part (i.e., the balloon). The expansions are generated by uniformly distributed pressures acting on the inner wall of the balloon.

Figure 3a and b presents the numerical setup. The backbone structure and balloon are separately modeled and concentrically assembled, and they are, respectively, meshed by structural cells and structural-tet coupled cells. Their bottom surfaces are fixed and supported in the same datum. It is

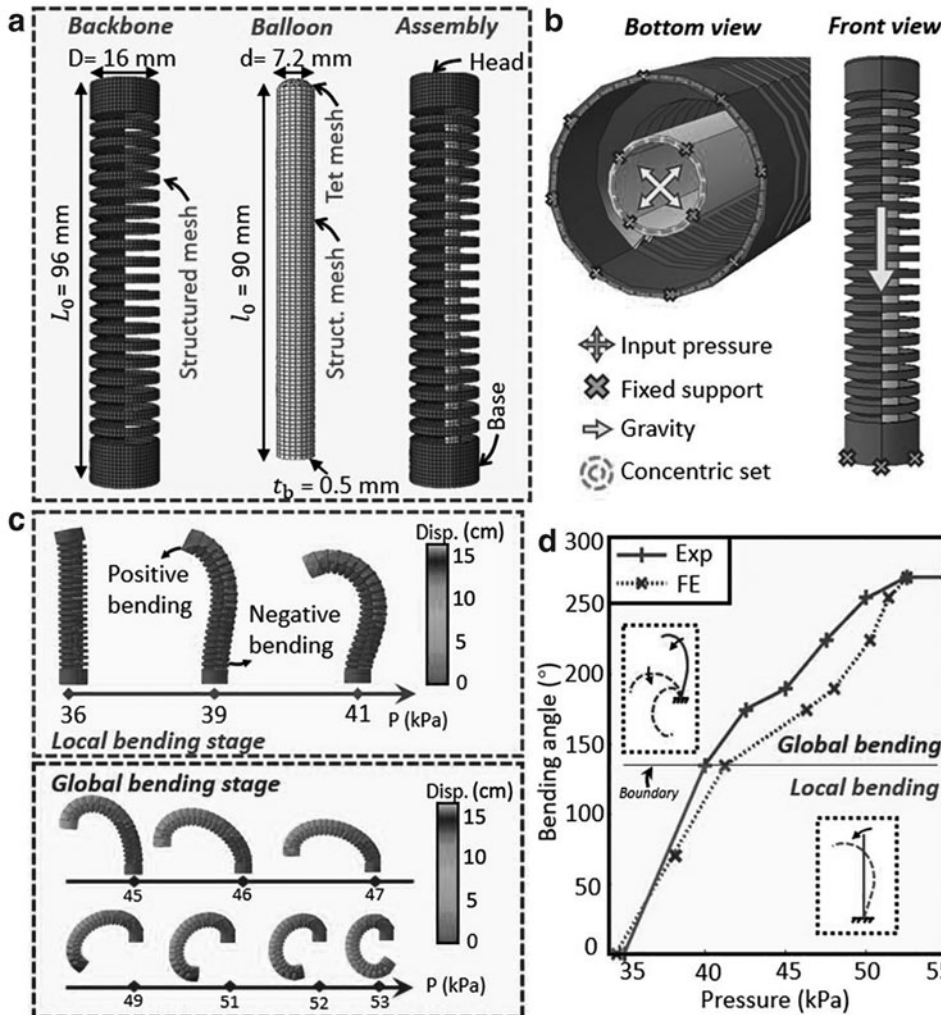


**FIG. 3.** The numerical setup and results: (a) structures, dimensions, and mesh methods of the numerical model, (b) boundary condition setups of the numerical model, (c) numerical results showing bending performances that can be divided into the local bending stage and the global bending stage according to bending statuses, and (d) comparisons between the numerical and experimental results regarding the pressure-bending angle relationships, which show satisfactory agreements.

worth pointing out that although TPU performs material properties between the elasticity and the hyperelasticity, in this case, TPU works at an early stress-strain stage and thus can be regarded as an isotropic elastomer. In addition, to reduce computational costs, the Neo-Hookean model is applied to calculate the hyperelastic performances of the balloon with acceptable calculation accuracy. The explicit dynamic solver is applied to calculate the nonlinear contact phenomenon, and the full contact method is considered to define the interaction characteristics. Detailed parameters of the numerical model are listed in Table 1.

### Numerical results

The experimental data validate the numerical results (Fig. 3d) in a pressure range of 35–55 kPa, and satisfactory agreement is obtained (see further comparisons in Supplementary Data). It should be noted that the accuracy of numerical predictions is affected by material parameter values and the order of the hyperelastomer function.

It can be seen in Figure 3c and d, based on bending performances, that this period can be divided into two bending stages that are the local bending stage and the global bending stage. In the local bending, actuators perform bending tendencies in inconsistent directions. The lower end of the actuator performs motions bending to the ribs side, while its higher section performs motions bending to the backbone side. This stage ends when the bending angle reaches about 140°. Then the global bending stage starts, during which actuators perform bending tendencies in a consistent bending direction. During this period, on the contrary, deformations of the lower end contribute most to the overall bending, while the higher section tends to perform displacements with the deformed shape at the end of the former stage. It should be noted that the above-mentioned bending stages can be visually identified from the pressure-bending angle relationship. During the local bending stage, the relationship of the pressure-bending angles presents well linearity, and during the global bending stage, it shows a logarithmic trend.

The mechanical responses of the backbone structure and the balloon are separately analyzed to investigate the interaction mechanism. As mentioned, in the separation stage, the backbone structure bends itself due to its structural asymmetry in response to gravity. Figure 4a presents the backbone's free oscillation phenomenon, a simple harmonic motion with decreasing amplitudes in a  $[-80, -10]^\circ$  range of bending angles. This process stops when the backbone structure stabilizes at the bending angle of  $-40^\circ$ . It should be noted that with the interaction of the unexpanded balloon that acts its weight on the inner surfaces of ribs, the bending angle at stabilized condition will be reduced (see actual stabilized bending in Fig. 2c).

In terms of the backbone part of the interaction, its mechanical responses, which refer to the relationship between the deformed gap angles  $\theta_G$  and the gap number, are presented in Figure 4b. We numbered gaps of the backbone from bottom to top. In the pressure range of  $[0, 35]$  kPa, the 1st to 14th gaps experienced the processes of reducing to a negative value and then returning to values of  $\sim 0^\circ$ , including the separation stage and the insufficient interaction stage, respectively. In the density plot, regions showing the local and global bending can also be visually identified during the pressure

range of  $[35, 50]$  kPa. Two areas framed by blue and red in Figure 4b exhibit different kinematic characteristics: In the local bending stage, the deformed gap angles are only sensitive to the pressure in the 15th to 20th gaps and are globally sensitive to the pressure in the global bending stage. Note that the first and second gaps significantly contribute to the global bending. Moreover, this effect can be reduced by adjusting the dimensions of the inner balloon and the backbone structure. It can also reduce the likelihood of ruptures and increase the average burst pressure of the actuator.

In terms of the balloon part of the interaction, its expansion responses, which refer to the relationships between the pressures and the axial and radial expansion ratios, are presented in Figure 4c. In the separation and insufficient interaction stage, expansion ratios freely and linearly develop with pressure. Once the balloon fully contacts the inner surfaces of the backbone structure, namely in the local bending stage, the radial expansion ratio remains linear while the axial expansion ratio increases with a higher developing speed than before. It reveals the fact that bending motions are linear during this stage. Thereafter, in the global bending stage, ribs cannot prevent the balloon from expanding outward, and thus, the radial and axial expansion ratios continue increasing monotonically till failures happen.

Further understanding of the interaction phenomenon can be learned from the stress responses to the pressure, which are shown in Figure 4d. Stresses of the backbone structure and balloon keep increasing freely in the separation stage. However, the insufficient interaction release stresses on the actuator due to it recovering to the original upright shape. Then in the local bending stage, as the elongations of the balloon, its overall stresses are released, performing steady motions. After that, stresses continue increasing in the global bending when the maximum stresses of the backbone and balloon exist at the backbone-ribs interfaces and the first gap. It should be noted that the local bending stage is generated by the difference caused by ribs to the length of force arms. Due to the stress accumulation, the maximum stress is finally transformed to the bottom of the actuator. Thus, the global bending stage occurs with the stress concentration at the 1st–2nd gaps.

### Parametric Study

To explain the derivation of the system instability and the method to overcome it, we conducted parametric studies according to the experimental testing with different geometry setups, which contain the hardness of the backbone (shore hardnesses of 30 A, 60 A, and 90 A), the radius of the balloon (3 and 3.6 cm), and the thickness of the balloon (1 layer and 2 layers). It should be noted that, limited to the fabrication technology, it is difficult to vary the parameters in a small range. Therefore, the numerical model validated in the previous section is applied to mechanically understand the parametric effects on the system instability in a small variation range. Moreover, 14 different types of backbone geometric designs are further investigated, considering the quantity of bones, slopes of bone shape, axial distributions of bones, and circumferential distributions of bones.

Figure 5a presents the experimental case table for the parametric study and the corresponding results. Deriving from different mechanical conditions, three types of system

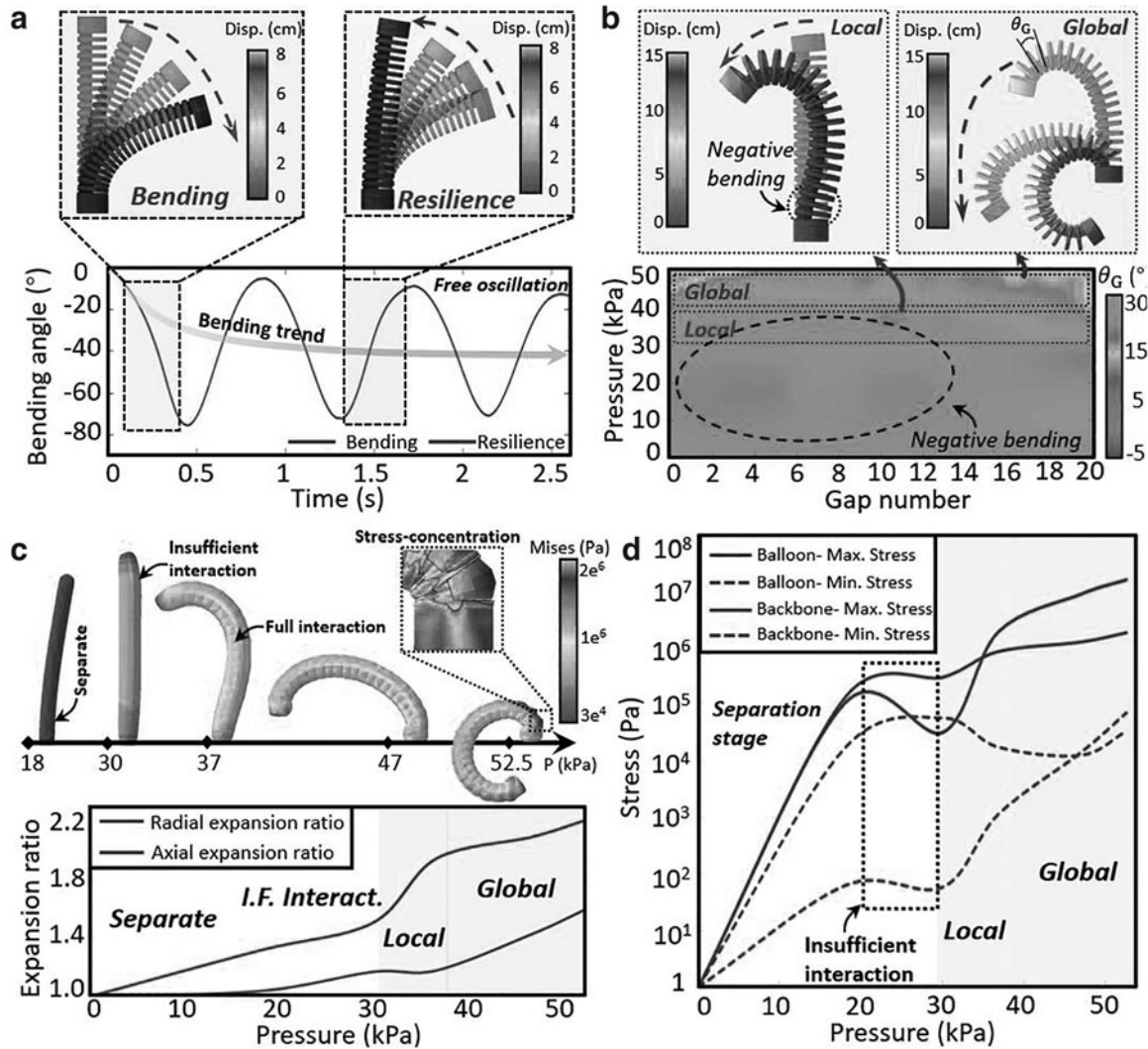


**FIG. 4.** Nonlinear interaction phenomenon analyses: (a) the free oscillation phenomenon of the backbone structure generated by the structural asymmetric stress responses to gravity, (b) the interaction performances of the backbone structure and the density plot showing the relationship between the gap numbers, pressures, and bending angles, (c) the interaction performances of the balloon and the relationships between the pressures and expansion ratios regarding the radial and axial expansion ratios, respectively, (d) relationships between the pressures and stresses regarding the backbone structure and balloon, respectively.

instability performances are observed, which are interaction failure, losing control, and overload.

Regarding the interaction failure, it derives from the over-soft backbone structure that cannot prevent the balloon from expanding. The strongly nonlinear interaction phenomenon relies on the backbone's restriction on the balloon. The interaction will stop functioning when the ribs are over-soft, leading to the balloon expanding out between neighboring ribs.

As displayed on the curve shown in Figure 5a, the interaction failure appears as a sudden bending change. Regarding losing control, it is a type of instability between failure and normal function. It drives by the unsatisfactory stress-conduct ability of the backbone structure due to the insufficient hardness (namely stiffness). The balloon expansion interacts with the ribs locally, which cannot be conducted to the top region leading to the losing control phenomenon. Figure 5b compares the losing control condition and the normal functioning condition. Regarding the overload, as an

opposite extreme, it derives from the over-thick balloon that is difficult to be expanded with the regular pressure input (0–70 kPa). Even if it could be actuated with higher air pressure, the conversion efficiency of pressure input to resulting payloads is unsatisfactory. It should be noted that connection bursts are observed when the system is overloaded (Fig. 5b).

As shown in Figure 5a by the arrows, the interaction failure can be overcome by adjusting the backbone's stiffness. The radius and stiffness simultaneously lead to the losing control phenomenon. To overcome the overload, the thickness (also stiffness) should be suitably arranged. The solid blue curve presents a parametric setup leading to a stable and satisfactory interaction phenomenon. It performs a linear relationship between the pressure and bending angle, which can be easily applied and predicted.

To further understand the parametric effects on the system instability in a small variation range, the numerical analysis is conducted by applying the validated numerical model.



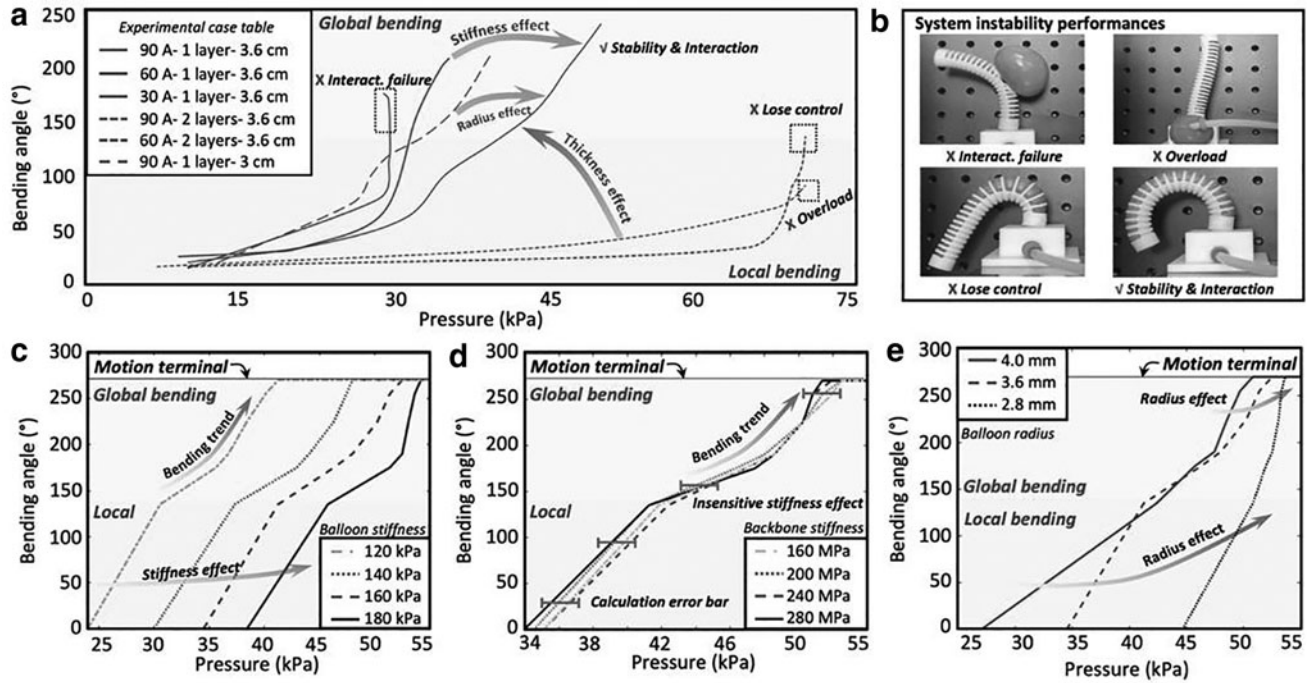


**FIG. 5.** The parametric study: (a) experimental results illustrating the instability derivations and methods to overcome it, (b) system instability performances, including the interaction failure, overload, and losing control, (c) pressure-bending relationships with the balloon stiffnesses  $C_{10}$  of 120, 140, 160, and 180 kPa, (d) pressure-bending relationships with the backbone stiffnesses  $E_B$  of 160, 200, 240, and 280 MPa, (e) pressure-bending relationships with the balloon diameter  $d$  of 8.0, 7.2, and 5.6 mm.

Table 2 presents the numerical case table for the parametric study. The stiffness of the balloon is first considered because the balloon is the actuation source of the PEBS, and its stiffness directly determines the system stability. It can be seen in Figure 5c, as the stiffness of balloons changes, the bending performances of actuators show a linear trend: the overall bending trends remain the same, and the start and end time of the actuation processes are advanced as the stiffnesses decrease. Therefore, we can select the corresponding balloon stiffness  $E_b$  to allow the actuator to work in a linear period by prearranging the operating pressure range (i.e., the period, including the local and global bending stages).

In terms of the backbone stiffness effects (Fig. 5d), the driving performances fluctuate in an acceptable interval in the selected stiffness range. Namely, the system instability is not derived from changes in the backbone stiffness  $E_B$  in a small range.

**TABLE 2. NUMERICAL CASE TABLE OF THE PARAMETRIC STUDY**

Case Num.	$C_{10}$	$E_B$	$d$ (mm)
1	$1.6 \times 10^5$	$2 \times 10^8$	7.2
2	$1.4 \times 10^5$	$2 \times 10^8$	7.2
3	$1.2 \times 10^5$	$2 \times 10^8$	7.2
4	$1.8 \times 10^5$	$2 \times 10^8$	7.2
5	$1.6 \times 10^5$	$1.6 \times 10^8$	7.2
6	$1.6 \times 10^5$	$2.4 \times 10^8$	7.2
7	$1.6 \times 10^5$	$2.8 \times 10^8$	7.2
8	$1.6 \times 10^5$	$2 \times 10^8$	5.6
9	$1.6 \times 10^5$	$2 \times 10^8$	2.8

Based on the regularity we learned from the studies above, we further focus on changing the diameters of the balloon. As shown in Figure 5e, as a main factor of the nonlinear interaction phenomenon, the balloon diameter directly affects the stability of the entire actuation process. With the original diameter ( $d = 7.2$  mm), actuators perform linear and nonlinear kinematic characteristics in the local bending and the global bending stages. When  $d$  increases to 8 mm, these motional characteristics will be more pronounced, and the corresponding working pressure range will be enlarged. This setting method allows the entire actuation process to be more accurately controlled with a larger independent variable interval. When  $d$  decreases to 5.6 mm, there are no longer significant differences between kinematic characteristics (i.e., linearity and nonlinearity) in the local and global stages and a smaller independent variable interval to control the motions of actuators.

From these effects, we can learn that the system instability mainly derives from the influence of the balloon geometric parameters on the nonlinear interaction phenomenon: the increase of the balloon diameter shortens the separation and insufficient stage and performs global-dominated motions. In contrast, the decrease of the balloon diameter performs local bending-dominated motions with more flexible and more nonlinear motions. It should be noted that although the system instability can be overcome by increasing the diameter of the balloon, setting an excessively large diameter will limit the system flexibility and further perform motions with large radii.

By combining proper backbone stiffness, balloon stiffness, and radius, the system instability of actuators can be overcome. To provide a further discussion on backbone geometries, 14 types of backbone designs are investigated



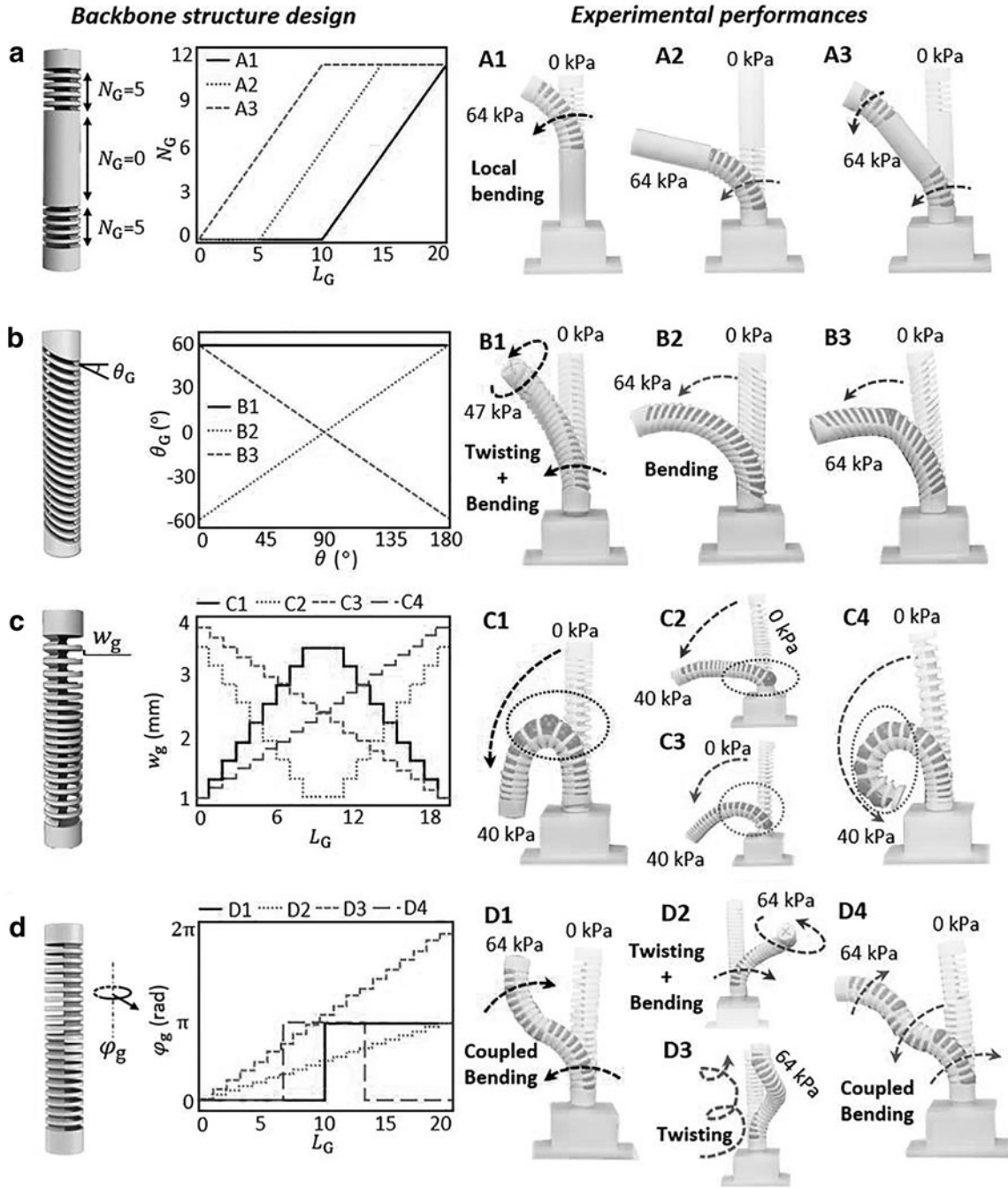


**FIG. 6.** The parametric study on the geometric designs of the backbone structures. (a) Quantity of ribs leading to variable stiffness effects of PEBS. (b) Slopes of rib shapes leading to the twisting-bending coupled motion and controlled potential failure regions. (c) Axial distribution of ribs leading to various types of motions caused by different critically bent regions. (d) Circumferential distribution of ribs leading to preprogrammed bending and twisting motions.

(Fig. 6). The backbone designs are considered from 4 perspectives, that are, the quantity of ribs, slopes of rib shapes, axial distribution of ribs, and circumferential distributions of ribs, respectively. Detailed designs are shown in the two left columns of Figure 6a to d. Note that  $L_G$ ,  $N_G$ ,  $\theta_G$ ,  $\theta$ ,  $w_g$ , and  $\varphi_g$  denote the location of ribs (numbered from bottom to top), accumulated number of ribs, slope angle of rib shape, circumferential angle over the rib, gap distance between neighboring ribs, and orientation of ribs, respectively.

Considering the quantity of ribs, A1, A2, and A3 are designed with top-gathered, bottom-gathered, and both sides gathered ribs, respectively (Fig. 6a). Local bendings are observed at the corresponding gathered regions, which proved that the PEBS could be endowed with the variable stiffness characteristic. The A3 design performs joint-bending motions that can be further developed into robotic fingers (hands). Considering side ratios of rib shapes, B1, B2, and B3 are designed with 60°, V-shaped, and vertically

reversed V-shaped ribs, respectively (Fig. 6b). The twisting-bending coupled motion is observed in the B1 design, resulting from the inhomogeneous deformation led by the circumferential asymmetric structure. B2 and B3 control the potential interaction failure location. V-shaped design (i.e., B2) provides a potential failure space at  $L_G = 2$  (the bottom second gap), while the vertically reversed design (i.e., B3) provides a potential failure space at  $L_G = 12$ . This phenomenon is a result of the accumulation of upward friction caused by the growing trend of the balloon.

Considering the axial distribution of ribs, C1–C4 are designed with both-sides-densed, middle-densed, top-densed, and bottom-densed rib distributions, respectively (Fig. 6c). Experimental performances imply that the axial distribution of ribs controls the location of critically bent regions. The rarely distributed region provides the space for the balloon's critical expansions. Regarding the circumferential distribution of ribs, shown in Figure 6d, designs with sudden changes in rib distributions perform coupled bending effects (e.g., D1 and D4); on the contrary, designs with continuous changes of rib distributions perform twisting effects (e.g., D2 and D3).

The parametric study on the backbone geometry provides the knowledge to make use of potential failures, which can be transformed into unique motion characteristics, such as coupled bending, twisting, and bending-twisting coupled motion. Till now, by considering the balloon property, backbone material property, and geometric design, the system instability can be overcome and used to perform various types of actuator motions. The system instability, their corresponding derivations, methods to overcome them, and potential functions of making use of these instabilities are summarized in Table 3 (see Supplementary Video S3).

## Applications

After investigating derivations of system instabilities and clarifying the corresponding overcome methods, PEBS can perform their expected advantages: the lightweight with high payloads, satisfactory modularization ability, and delicate motions with safe human interaction ability. Biomedical applications (e.g., endoscopy, surgery operator, and assistant) propose challenging requirements for soft robots, such as accurate motion control, operation safety, integration of diversified tools, and collaborative ability. Meeting all the

required abilities, PEBS is expected to be a competent role. In this section, to validate the applicability of PEBS, we apply PEBS to conduct laryngoscopy, build a PEBS library for robot-arm modularization, and operate a collaboration surgery.

The laryngoscope is a type of rigid biomedical tool ( $\sim 350$  g) for laryngeal diagnosis or surgery, which is directly attached to the delicate and flexible surface of the mouth. A lightweight and flexible laryngoscope will improve patient comfort during the treatment. As shown in Figure 7a, a PEBS with the A1 structure is designed into a soft laryngoscope ( $<15$  g), which is integrated with an image sensor (with a light source, CMOS camera-OV6946, OmniVision, CA, USA). Note that the sensor's wire can be easily threaded through the PEBS and will not be damaged by the inflating balloon. An oropharyngeal phantom is applied to test the functionality of the PEBS soft laryngoscope.

Figure 7b shows real-time images captured by the image sensor. The laryngoscope was flatly attached to the tongue at  $t = 0$ , when a clear outline between the tongue and soft palate can be observed (Fig. 7b-i). With a slight bending ( $\sim 15^\circ$ ) in 10 s, the laryngoscope got over the tongue and observed the esophagus (Fig. 7b-ii). Continuing bending, the epiglottis and glottis were observed in order (Fig. 7b-iii and -iv). Note that during the entire process, the input pressure was lower than 65 kPa, which is safe for human interaction (see Supplementary Video S4).

Taking advantage of satisfactory modularization, a PEBS library is built for operating further complex tasks. The library contains the afore-reported 14 types of backbone designs. A robot arm (Kuka LBR Med 7 R800) is applied as the robotic platform (Fig. 7c). A three-dimensional printed install flange contains three ports where balloons are preinstalled in. The PEBS can be modularly installed with alignment and docking. As shown in Figure 7d, a PEBS-based grasper can lift a tennis ball that is 4.8 times heavier than the total mass of the three PEBS actuators. For the other extreme, the grasper can delicately grasp an M4 screw with three A1 PEBS designs. A ping-pong ball can be twisted  $90^\circ$  by deploying three D2 PEBS designs. The PEBS library demonstrates satisfactory modularization ability, which helps avoid complex fabrication processes (e.g., coiling, molding, and so on) and professional repair techniques after being damaged.

The PEBS library provides a broad space for soft actuators to integrate diversified biomedical tools, just like the well-known da Vinci surgical robotic system. The robot arm-equipped PEBS system is applied to operate a debridement

TABLE 3. SUMMARIZATION OF SYSTEM INSTABILITY CATEGORIES, THEIR DERIVATIONS, OVERCOME METHODS, AND POTENTIAL FUNCTIONS OF INSTABILITIES

<i>System instability category</i>	<i>Derivation</i>	<i>Overcome method<sup>a</sup></i>	<i>Potential function of instability<sup>b</sup></i>
Interaction failure	● Oversoft backbone stiffness	→ Backbone hardness in 60–90 A	MIS: <i>in vivo</i> support
Overload	● Overlarge backbone gaps	→ Gap distance $<1.9$ times bone width	Rupture protection
	● Over thick/stiff balloon	→ Balloon stiffness in 120–180 kPa	Preprogrammed motion
		→ Balloon thickness in a single layer (0.5 mm)	
Lose control	● Insufficient backbone stiffness	→ Backbone stiffness in 160–280 MPa	
	● Insufficient balloon radius	→ Balloon radius in 0.7–0.9 times of backbone radius	

<sup>a</sup>Overcome methods protect PEBS soft actuators from occurring system instabilities in an input pressure range of 0–64 kPa, where the actuators can realize preprogrammed motions.

<sup>b</sup>Potential functions of instability: instead of avoiding occurring system instability, these instabilities can also be potentially applied in certain scenarios.

MIS, minimally invasive surgery; PEBS, pneumatically elastic backbone structure.

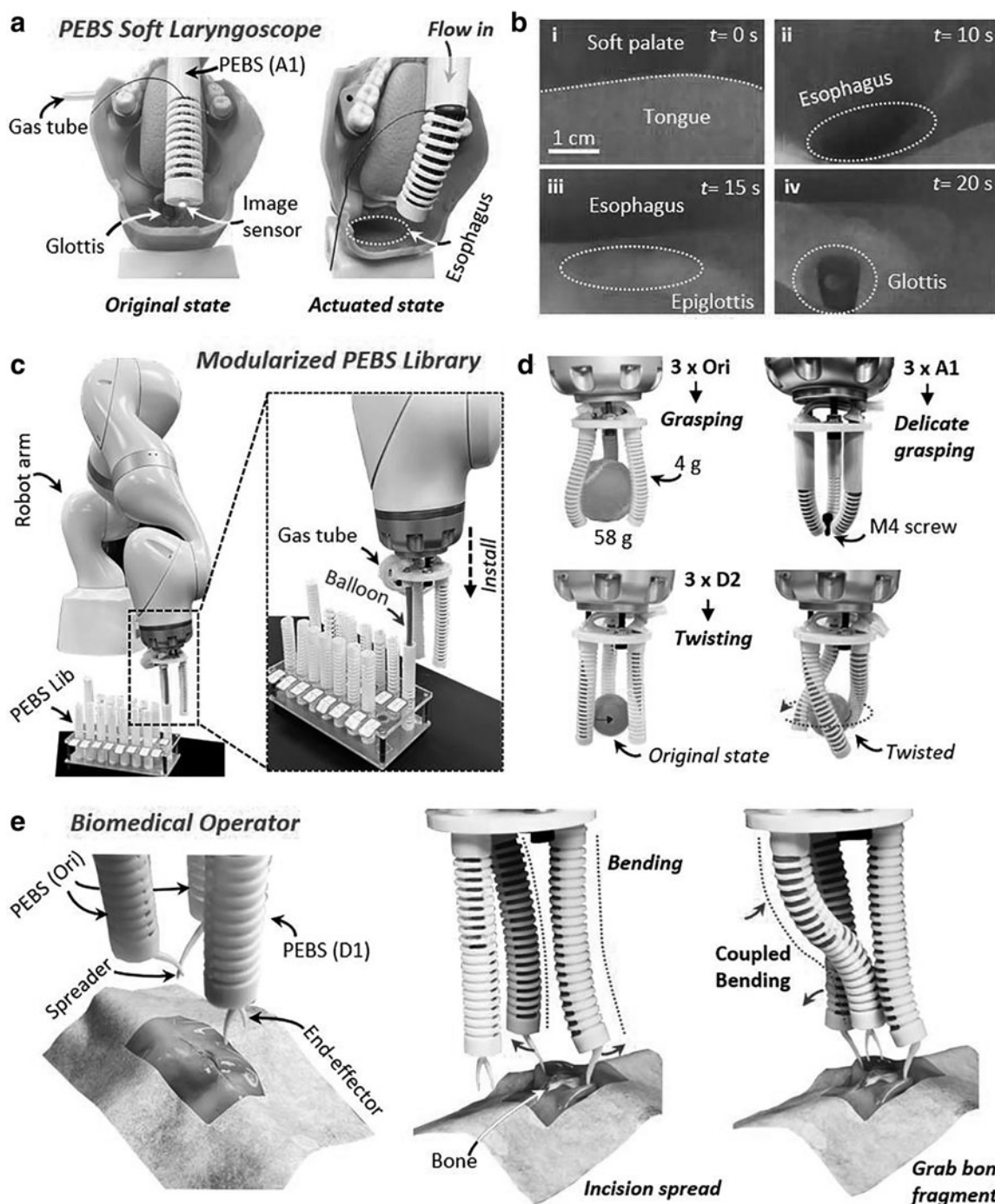


**FIG. 7.** Applications of PEBS demonstrate unique advantages of accurate controllability, operation safety, modularization ability, and collaborative ability. (a) A PEBS soft laryngoscope that can operate laryngeal diagnosis. (b) Real-time images captured by the integrated image sensor. (c) Modularized PEBS library that can be installed onto a robot arm. (d) A PEBS grasper that can operate various grasping tasks. (e) The PEBS system can be potentially applied to operate a debridement.

(e.g., grab bone fragments). The system contains two original PEBS designs for incision spread and a D1 PEBS design for grabbing bone fragments (Fig. 7e). A tissue model is made of silicon rubber and stained with acrylic paint, which covers an ossa antebrachii model. The robot arm was first positioned over the incision and slowly approached until the spreaders touched the incision. The end-effector performed coupled bending motions when the bone fragments appeared by the incision spread. The demonstrated application provides possibilities for

applying soft actuators to operate remote surgeries (see Supplementary Videos S5–S6).

The reported biomedical applications demonstrate the unique advantages of PEBS: accurate controllability, operation safety, modularization ability, and collaborative ability. Despite biomedical purposes, the PEBS can also be designed into biomimetic robots (i.e., a soft crawling robot; Supplementary Videos S1, S2), demonstrating well mobility of PEBS (with an average speed of  $\sim 0.6$  cm/s).

## Conclusions

This study developed a type of modular lightweight (<80 g) pneumatic inner balloon and backbone structured soft actuators with satisfactory modularization ability and biomedical applicability. We focus on the influence factors on actuation processes: system instability and the strongly nonlinear interaction phenomenon. Experimental, theoretical, numerical, and parametric studies are conducted. Experiments were conducted to obtain the bending characteristics and the load capacity (~20 times the self-weight). A simplified theoretical model was established to estimate the values of generated forces. To explain the mechanism of the strongly nonlinear interaction phenomenon during the actuation process, a numerical model was investigated and validated by experimental results with satisfactory agreements.

Furthermore, parametric studies are conducted based on the numerical model to learn the derivation of the system instability and the methods to overcome it. After overcoming the system instability and taking advantage of the nonlinear phenomenon, in the end, we applied the PEBS to design a soft laryngoscope, a modularized PEBS library, and a PEBS system to conduct remote surgery. The accurate controllability, operation safety, modularization ability, and collaborative ability of the PEBS were thus validated.

Future studies could focus on applying the PEBS to other applications, such as biomedical devices (e.g., endoscopy), detective devices (e.g., narrow channel explorer), and smart operators (e.g., soft fingers or hands). In the applications of biomedical engineering, the reduction of PEBS sizes can enable the realization of continuous soft actuators for *in vivo* tasks. When viewed from the perspective of field exploration, increasing the DOF of PEBS could enable more precise and adaptable movements. From the standpoint of grasping applications, exploring novel structure designs has the potential to enhance the actuation capabilities of graspers, such as more delicate and complex actuations, making them more intricate and refined.

## Acknowledgments

This work was supported by the National Key R&D Program of China under Grant 2018YFB1307700 (with subprogram 2018YFB1307703) from the Ministry of Science and Technology (MOST) of China, Hong Kong Research Grants Council (RGC) Collaborative Research Fund (CRF C4026-21GF), General Research Fund (GRF 14216022), the key project 2021B1515120035 (B.02.21.00101) of the Regional Joint Fund Project of the Basic and Applied Research Fund of Guangdong Province, and Singapore Academic Research Fund under Grant R397000353114. Y.Y. acknowledges the China Scholarship Council scholarships (202006320349) at the Ministry of Education (MOE), China.

## Supplementary Material

Supplementary Data  
Supplementary Video S1  
Supplementary Video S2  
Supplementary Video S3  
Supplementary Video S4  
Supplementary Video S5  
Supplementary Video S6

## References

1. Lee C, Kim M, Kim YJ, et al. Soft robot review. *Int J Control Autom Syst* 2017;15(1):3–15.
2. Shepherd RF, Ilievski F, Choi W, et al. Multigait soft robot. *Proc Natl Acad Sci USA* 2011;108(51):20400–20403.
3. Hirose S, Umetani Y. The development of soft gripper for the versatile robot hand. *Mech Mach Theory* 1978;13(3):351–359.
4. Wang Z, Torigoe Y, Hirai S. A prestressed soft gripper: Design, modeling, fabrication, and tests for food handling. *IEEE Robot Autom Lett* 2017;2(4):1909–1916.
5. Wang W, Ahn S-H. Shape memory alloy-based soft gripper with variable stiffness for compliant and effective grasping. *Soft Robot* 2017;4(4):379–389.
6. Zaidi S, Maselli M, Laschi C. Actuation technologies for soft robot grippers and manipulators: A review. *Curr Robot Rep* 2021;2(3):355–369.
7. Dou W, Zhong G, Cao J. Soft robotic manipulators: Designs, actuation, stiffness tuning, and sensing. *Adv Mater Technol* 2021;6(9):2100018.
8. Khomami AM, Najafi F. A survey on soft lower limb cable-driven wearable robots without rigid links and joints. *Robot Autonom Syst* 2021;144:103846.
9. Xia Y, He Y, Zhang F. A review of shape memory polymers and composites: Mechanisms, materials, and applications. *Adv Mater* 2021;33(6):2000713.
10. Bartlett NW, Tolley MT, Overvelde JTB, et al. A 3D-printed, functionally graded soft robot powered by combustion. *Science* 2015;349(6244):161–165.
11. Yang Y, Hou B, Chen J, et al. High-speed soft actuators based on combustion-enabled transient driving method (TDM). *Extreme Mech Lett* 2020;37:100731.
12. Wang H, Yang Y, Lin G, et al. Untethered, high-speed soft jumpers enabled by combustion for motions through multiphase environments. *Smart Mater Struct* 2020;30(1):015035.
13. Seok S, Onal CD, Cho K, et al. Meshworm: A peristaltic soft robot with antagonistic nickel titanium coil actuators. *IEEE/ASME Trans Mech* 2013;18(5):1485–1497.
14. Chen B, Zhu Y, Zhao J, Cai H, (eds). Design of a prototype of an adaptive soft robot based on ferrofluid. In: 2015 IEEE International Conference on Robotics and Biomimetics (ROBIO). December 6–9, 2015.
15. Wang X, Yang B, Tan D, et al. Bioinspired footed soft robot with unidirectional all-terrain mobility. *Mater Today* 2020;35:42–49.
16. Du Y, Xu M, Dong E, et al., (eds). A novel soft robot with three locomotion modes. In: 2011 IEEE International Conference on Robotics and Biomimetics. December 7–11, 2011.
17. Huang W, Xu Z, Xiao J, et al. Multimodal soft robot for complex environments using bionic omnidirectional bending actuator. *IEEE Access* 2020;8:193827–193844.
18. Shi C, Luo X, Qi P, et al. Shape sensing techniques for continuum robots in minimally invasive surgery: A survey. *IEEE Trans Biomed Eng* 2017;64(8):1665–1678.
19. Li Z, Ren H, Chiu PWY, et al. A novel constrained wire-driven flexible mechanism and its kinematic analysis. *Mech Mach Theory* 2016;95:59–75.
20. Gong Z, Fang X, Chen X, et al. A soft manipulator for efficient delicate grasping in shallow water: Modeling, control, and real-world experiments. *Int J Robot Res* 2020;40(1):449–469.
21. Mohamed A, Shaw-Sutton J, Green B, et al. Soft manipulator robot for selective tomato harvesting. *Precis Agric* 2019;1:799–805.

22. Tolley MT, Shepherd RF, Karpelson M, et al., (eds). An untethered jumping soft robot. In: 2014 IEEE/RSJ International Conference on Intelligent Robots and Systems. IEEE; 2014.
23. Al-Fahaam H, Davis S, Nefti-Meziani S, (eds). Wrist rehabilitation exoskeleton robot based on pneumatic soft actuators. In: 2016 International Conference for Students on Applied Engineering (ICSAE). IEEE; 2016.
24. Hawkes EW, Blumenschein LH, Greer JD, Okamura AM. A soft robot that navigates its environment through growth. *Sci Robot* 2017;2(8):eaan3028.
25. Bern JM, Banzet P, Poranne R, Coros S, (eds). Trajectory Optimization for Cable-Driven Soft Robot Locomotion. Robotics: Science and Systems; 2019.
26. Wang H, Zhang R, Chen W, et al. A cable-driven soft robot surgical system for cardiothoracic endoscopic surgery: Preclinical tests in animals. *Surg Endosc* 2017;31(8):3152–3158.
27. Chen F, Xu W, Zhang H, et al. Topology optimized design, fabrication, and characterization of a soft cable-driven gripper. *IEEE Robot Autom Lett* 2018;3(3):2463–2470.
28. Jin B, Song H, Jiang R, et al. Programming a crystalline shape memory polymer network with thermo- and photo-reversible bonds toward a single-component soft robot. *Sci Adv* 2018;4(1):eaao3865.
29. Kheirikhah MM, Rabiee S, Edalat ME, (eds). A review of shape memory alloy actuators in robotics. In: *Robot Soccer World Cup*. Springer: Berlin, Heidelberg; 2010.
30. Rodrigue H, Wang W, Han M-W, et al. An overview of shape memory alloy-coupled actuators and robots. *Soft Robot* 2017;4(1):3–15.
31. Walker ID. Continuous backbone “continuum” robot manipulators. *Int Sch Res Notices* 2013;2013:726506.
32. Laschi C, Cianchetti M, Mazzolai B, et al. Soft robot arm inspired by the octopus. *Adv Robot* 2012;26(7):709–727.
33. He B, Wang Z, Li Q, et al. An analytic method for the kinematics and dynamics of a multiple-backbone continuum robot. *Int J Adv Robot Syst* 2013;10(1):84.
34. Martinez RV, Branch JL, Fish CR, et al. Robotic tentacles with three-dimensional mobility based on flexible elastomers. *Adv Mater* 2013;25(2):205–212.
35. Jin H, Dong E, Xu M, et al. Soft and smart modular structures actuated by shape memory alloy (SMA) wires as tentacles of soft robots. *Smart Mater Struct* 2016;25(8):085026.
36. Feng H, Sun Y, Todd PA, Lee HP. Body wave generation for anguilliform locomotion using a fiber-reinforced soft fluidic elastomer actuator array toward the development of the eel-inspired underwater soft robot. *Soft Robot* 2020;7(2):233–250.
37. Sedal A, Bruder D, Bishop-Moser J, et al. A continuum model for fiber-reinforced soft robot actuators. *J Mech Robot* 2018;10(2):024501.
38. Stalin T, Thanigaivel NK, Joseph VS, Alvarado PV, (eds). Automated fiber embedding for tailoring mechanical and functional properties of soft robot components. In: 2019 2nd IEEE International Conference on Soft Robotics (RoboSoft). IEEE; 2019.
39. Xing Z, Zhang J, McCoul D. A super-lightweight and soft manipulator driven by dielectric elastomers. *Soft Robot* 2020;7(4):512–520.
40. Elena GM. Novel design of a soft lightweight pneumatic continuum robot arm with decoupled variable stiffness and positioning. *Soft Robot* 2018;5(1):1–17.
41. Frick A, Rochman A. Characterization of TPU-elastomers by thermal analysis (DSC). *Polymer Test* 2004;23(4):413–417.
42. Ismail H. Thermoplastic elastomers based on polypropylene/natural rubber and polypropylene/recycle rubber blends. *Polymer Test* 2002;21(4):389–395.
43. Herrera M, Matuschek G, Kettrup A. Thermal degradation of thermoplastic polyurethane elastomers (TPU) based on MDI. *Polymer Degradat Stabil* 2002;78(2):323–331.
44. Markarian J. Thermoplastic elastomer compounds continue upward trend. *Plast Add Compound* 2008;10(5):38–43.
45. Przybytek A, Kucińska-Lipka J, Janik H. Thermoplastic elastomer filaments and their application in 3D printing. *Elastomery*. 2016;20:33–39.
46. Xiao J, Gao Y. The manufacture of 3D printing of medical grade TPU. *Progr Add Manuf* 2017;2(3):117–123.
47. Choi J, Kwon O-C, Jo W, et al. 4D printing technology: A review. *3D Print Add Manuf* 2015;2(4):159–167.
48. Abaqus G. Abaqus 6.11. Dassault Systemes Simulia Corporation: Providence, RI, USA; 2011.

Address correspondence to:

*Hongliang Ren  
Department of Electronic Engineering  
The Chinese University of Hong Kong  
Hong Kong 999077  
China*

*E-mail: hren@cuhk.edu.hk, ren@nus.edu.sg*